ISSN (Print) 1226-1750
ISSN (Online) 2233-6656
Journal of Magnetics 23(4), 601-605 (2018) https://doi.org/10.4283/JMAG.2018.23.4.601

MR Compatible Digital Three-Dimensional Readout Detector using a Convergence of Cross Point and Dual-Ended Readout Methods

Seung-Jae Lee[1,2] and Cheol-Ha Baek[3]*

[1]*Department of Radiological Science, Dongseo University, Busan 47011, Republic of Korea*
[2]*Center for Radiological Environment & Health Science, Dongseo University, Busan 47011, Republic of Korea*
[3]*Department of Radiological Science, Kangwon National University, Samcheok 25949, Republic of Korea*

(Received 20 November 2018, Received in final form 18 December 2018, Accepted 19 December 2018)

We designed a magnetic resonance (MR) compatible depth-encoding detector using cross point and dual-ended readout methods with wavelength-shifting (WLS) fibers. To evaluate the performance of the novel detector module, we used the DETECT2000 simulation tool to model the transport of optical photons in the crystal array. The detector is composed of two layers of crystal arrays, three layers of WLS fiber arrays, and two sensor arrays. The identification of crystal pixels was determined by the cross point readout method using a digital positioning algorithm, and the depth information in each crystal pixel was measured by the dual-ended readout method. The average pixel identification accuracy was 93.5 % (range: 84.4 %-100 %).

Keywords : magnetic resonance, cross point readout, dual-ended readout, depth information, WLS fiber

1. Introduction

Positron emission tomography-magnetic resonance imaging (PET-MRI) is a hybrid medical imaging technique that dramatically increases the value of PET by providing an anatomical backdrop [1]. PET-MRI has traditionally been challenging because the photomultiplier tubes are affected by a magnetic field. Recently, research has focused on developing preclinical PET detectors using semiconductor detectors that are not affected by a magnetic field [2-4]. In preclinical PET, a long, thin scintillation crystal is used to provide high detection efficiency and good image quality [5]. However, these crystals increase the fraction of gamma rays obliquely incident on the detector surface, which gradually degrades the spatial resolution from the center to the periphery of the field of view (FOV) [6-8]. The degradation of the spatial resolution can be corrected so that the radial resolution is uniform throughout the FOV by measuring the depth of interaction (DOI) within the crystal [9]. Various DOI encoding designs have been proposed, namely the multi-layer detector, direct measuring detector, and dual-ended readout detector [10-12]. Multi-layer detectors are composed of multiple layers of scintillation crystal arrays and a single photosensor. The DOI is measured by pulse-shape discrimination, relative offset structure, and light sharing methods. Direct measuring detectors consist of several layers of crystal arrays, which are directly coupled to photosensors between crystal layers. Dual-ended readout detectors consist of a single crystal array and two photosensors connected to the ends of a crystal array. Our previously developed detector also can measure the DOI [13]. This detector was made up of several layers of crystal arrays and wavelength-shifting (WLS) fiber arrays. Because it was composed of several layers of crystal arrays, the three-dimensional positions were directly extracted. However, many photosensors were needed.

In this study, we designed a cost-effective and magnetic resonance (MR) compatible detector that reduced the number of photosensors through a convergence of the cross point and dual-ended readout methods and used semiconductor sensors for high resolution. Although fewer layers of WLS fiber arrays were required than in the previous detector, four DOI layers were still used. To evaluate the performance of the detector, the DETECT2000 [14] simulation tool was used to model transport of optical photons in the crystal array and WLS fibers.

©The Korean Magnetics Society. All rights reserved.
*Corresponding author: Tel: +82-33-540-3389
Fax: +82-33-540-3389, e-mail: baekch100@gmail.com

© 2018 Journal of Magnetics

2. Experimental Details

2.1. Design of a MR compatible digital three-dimensional detector module

The detector module consisted of two layers of scintillator arrays, three layers of WLS fiber arrays, and two sensor arrays. As shown in Fig. 1, the top and bottom surfaces of each scintillator array were coupled to WLS fiber arrays, which were arranged perpendicular to one another to direct the scintillation light in the X and Y directions. The end of the WLS fiber arrays was coupled to photosensors for the detection of scintillating light trapped in the fibers. Lutetium orthosilicate (LSO) crystals with a high stopping power and a high light yield were used to detect an annihilation gamma ray of 511 keV. The WLS fibers chosen for coupling to the LSO crystals were BCF91-A, because the absorption wavelength range of WLS fibers matches well with the LSO emission wavelength range [15]. The photosensors used S12572-50p Hamamatsu multi-pixel photon counters (MPPCs) [16] to measure light trapped by the WLS fibers. The MPPC dimensions were 3.85 mm × 4.35 mm with a 3 mm × 3 mm photosensitive area. Its spectral response has a range of 320-900 nm with a peak sensitivity wavelength at 450 nm (35 % quantum efficiency). The quantum efficiency of the WLS fiber reemission peak was approximately 32.5 %. An optical grease (refractive index: 1.465) was used as a coupling material for the detector module to reduce light loss caused by the different refractive indices between the LSO and WLS fibers, and between the WLS fibers and MPPC.

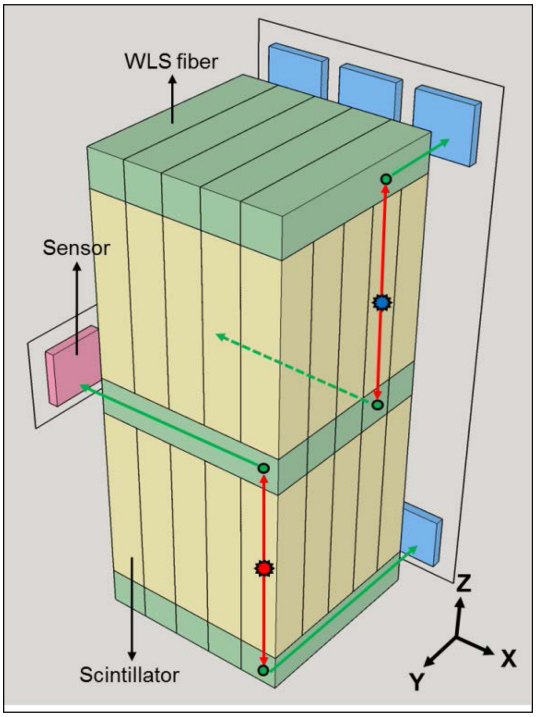

Fig. 1. (Color online) Geometry of the MR compatible three-dimensional readout detector module. The MPPCs are shown in blue (backward) and red (left). Light generated from the crystals (red and blue stars) moves in the directions of the green arrows.

The LSO crystal array in each layer consisted of 5 × 5 crystals, each of which measured 2 mm × 2 mm × 10 mm. Each WLS fiber layer was composed of 1 × 5 arrays, each of which measuring 2 mm × 10 mm × 2 mm. A total of nine MPPCs were used: 3 × 2 MPPCs in the X-Z plane and 3 × 1 MPPCs in the Y-Z plane.

2.2. Simulation Conditions

All LSO side surfaces (refractive index: 1.82) were painted with a reflection coefficient (RC) of 0.98; the other surfaces were optically coupled to the WLS fibers. All WLS fiber surfaces (refractive index: 1.6), except for those coupled to the LSO, were treated with a specular reflector of 0.98 RC. Gamma events were generated in all LSO crystals at evenly spaced points with 0.2 mm spacing in the X, Y, and Z directions. The number of light photons produced by the gamma ray interaction was calculated using the LSO light conversion efficiency for a 511 keV gamma ray, the WLS light absorption efficiency, and the probability that reemitted photons would shift to a longer wavelength in the WLS fiber. Light photons generated in the LSO were trapped in the WLS fiber where they were absorbed and reemitted in the WLS fiber and channeled toward the MPPC, enabling pixel identification and determination of depth information of the gamma interaction.

2.3. Three-dimensional positioning

Three-dimensional positioning was done through a depth measurement process after pixel identification. As shown in Fig. 2, the MPPCs of the X-Z and Y-Z planes consisted of three X, three Y, and three Z channels. The pixel identification of the X axis, Y axis, and the crystal layers were directly digitized using a digital positioning algorithm with the cross point readout [17]. The X position was determined from the combination of the three X channels. If the signal was only acquired by the X1 channel, the pixel that interacted with the gamma ray was the first pixel in the LSO array. If the signal was acquired by the X1 and X2 channels, the pixel was the second pixel. Thus, odd pixels were detected on a single X channel, whereas even pixels were detected on two X channels. The Y position was determined by the same process used to determine the X position. The deter-

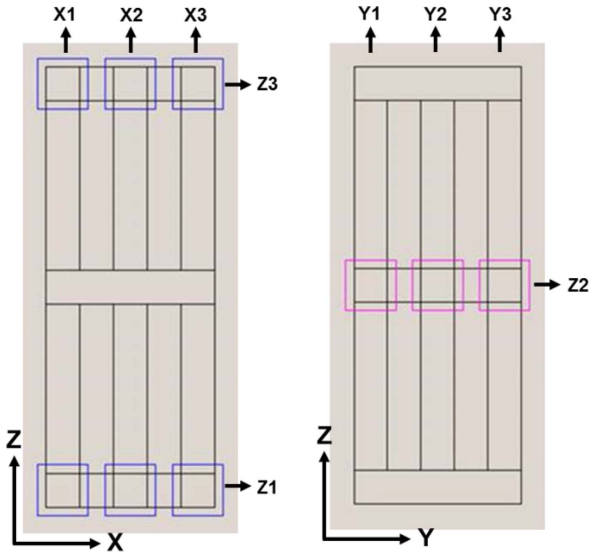

Fig. 2. (Color online) MPPC positions and multiplexed readout for each direction in the detector module.

mination of the crystal layer used the three Z channels. If the gamma ray interacted with the first layer, the signal was measured at the Z1 and Z2 channels, whereas if the gamma ray interacted with the second layer, the signal was acquired by the Z2 and Z3 channels.

The depth layer in each crystal pixel was simply determined from the ratio of the Z1 or Z3 signal and the total signal (Z1 + Z2 + Z3) using the dual-ended readout method. In the first crystal layer, if the value of the Z1 signal divided by the total signal was greater than 0.5, the depth layer was the first; otherwise it was second. Similarly, if the value of the Z3 signal divided by the total signal was less than 0.5, the depth layer was the third; otherwise it was fourth. Therefore, the three-dimensional position information of the four layers could be determined digitally

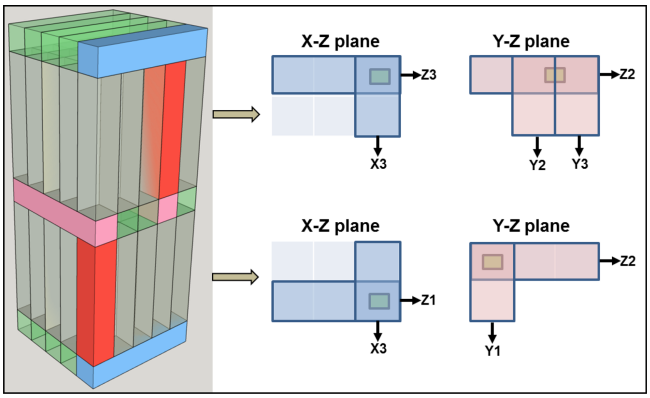

Fig. 3. (Color online) Data processing of red crystals using a cross point readout method with a digital positioning algorithm.

by comparing the signals acquired on each channel.

Figure 3 shows examples of pixel identification in the X and Y planes and crystal layer determination for the (5, 4, 2) pixel and the (5, 1, 2) pixel. In the (5, 4, 2) pixel, the light generated by a gamma photon was detected on the X3 and Z3 channels of the X-Z plane and the Y2, Y3, and Z2 channels of the Y-Z plane. For the (5, 1, 1) pixel, the light was detected on the X3 and Z1 channel of the X-Z plane, and the Y1 and Z2 channels of the Y-Z plane.

When the signal was detected on several channels, it was necessary to find the peak value and compare other signals with the peak value. A threshold was set to accurately identify the pixel and remove the low signals. Only channels with a signal above the threshold were used for pixel identification.

3. Results and Discussion

Figure 4 shows the data output channels from the red

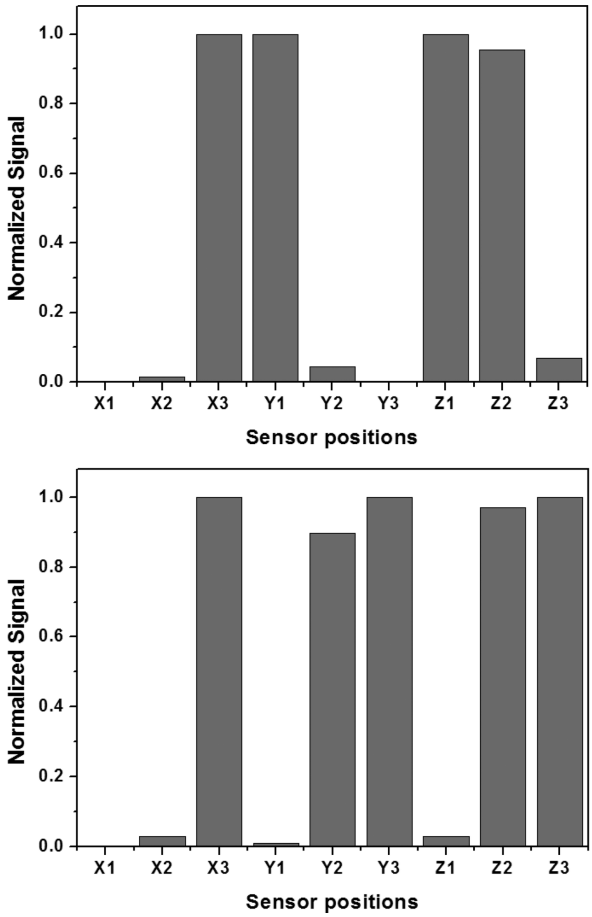

Fig. 4. Data outputs of the readout channels of the red crystals shown in Fig. 3. The top and bottom plots show the normalized data outputs of the (5, 1, 1) pixel and the (5, 4, 2) pixel, respectively.

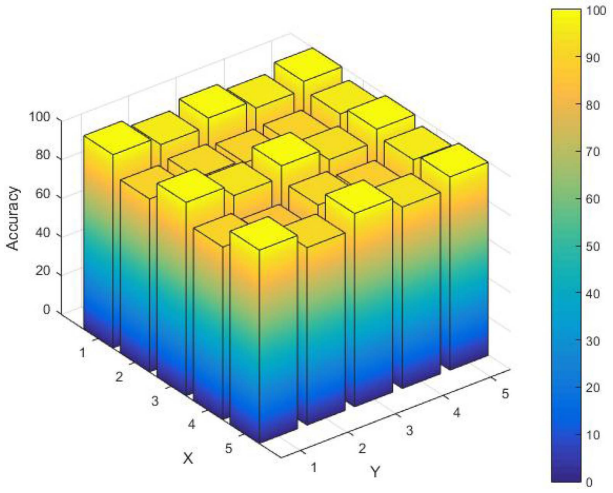

Fig. 5. (Color online) Pixel identification accuracy at the 80 % threshold.

crystals shown in Fig. 3. X1 to Y3 determine the X and Y positions, and Z1 to Z3 determine the crystal layer. The signal values are normalized by the peak values of each axis. The signals are mainly measured in the channels optically coupled to the crystals. Signals measured at other channels than those optically coupled to the crystals are not used due to the threshold in the digital positioning algorithm.

Figure 5 shows the pixel identification accuracy when the threshold of an 80 % value compared with the peak value was applied to all crystal pixels. Table 1 provides the pixel identification accuracy of all crystal pixels at an 80 % threshold. The average accuracy of all crystal pixels was 93.49 % (range: 79.8 % to 100 %). The accuracy of the even crystals, whose signals were divided, was lower than that of the odd crystals, whose signals were not divided. The crystals measured by dividing the signal from the four sensors, such as (2, 2) pixel, had the lowest pixel identification accuracy because the signal loss was relatively large as the signal was divided into several sensors.

Figure 6 shows the pixel identification accuracy at several thresholds, ranging from 10 %-90 %. Accuracy

Table 1. Pixel identification accuracy of all crystal pixels at an 80 % threshold.

Pixel No.	X1	X2	X3	X4	X5
Y1	100	95.68	100	95.4	100
Y2	86.8	84.35	89.82	87.8	94.13
Y3	100	93.19	100	93.2	100
Y4	86.58	79.8	90.18	84.6	93.97
Y5	100	90.52	100	91.2	100

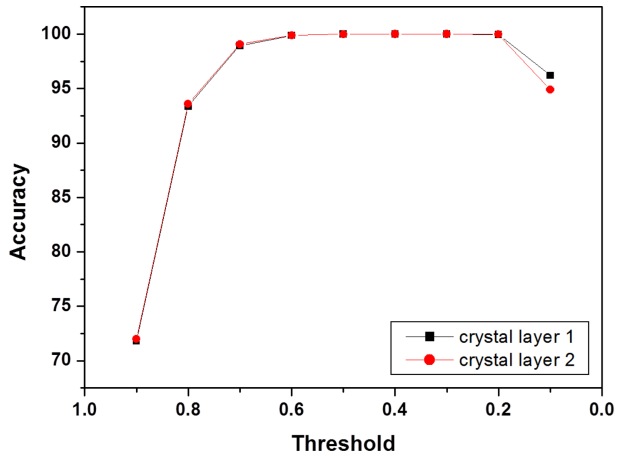

Fig. 6. (Color online) Pixel identification accuracy for several thresholds in all crystal layers.

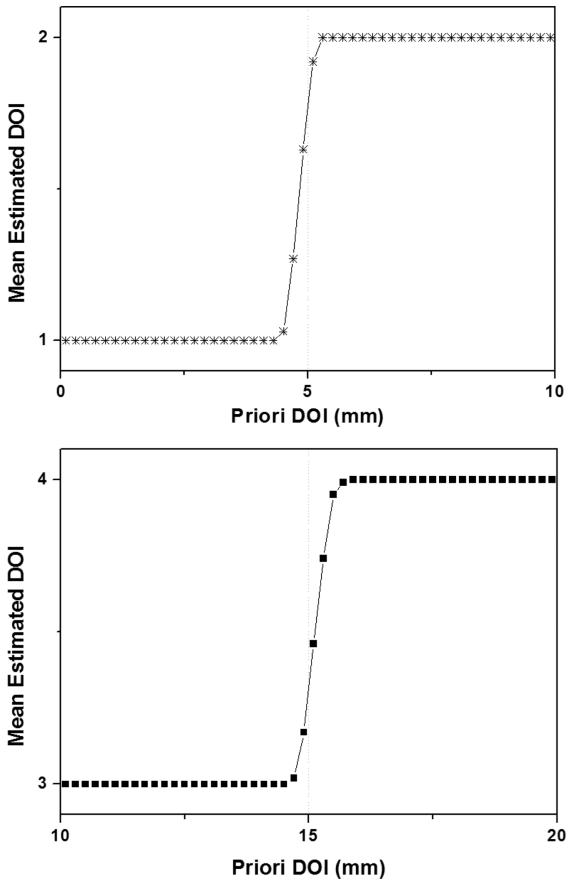

Fig. 7. DOI positioning results in each crystal layer. The horizontal axis is the true position from simulation input, and the vertical axis is the mean estimated position for different true positions.

exceeded 90 % at all thresholds, with the exception of the 90 % threshold. When the threshold is 10 %, it is difficult to distinguish between sensors with small signal values. So the accuracy was lower.

The mean estimated DOIs in each crystal layer are plotted as a function of the true position in Fig. 7. It can be seen that two DOI positions are clearly defined in each crystal layer. The position misclassification rate was measured over all pixels as 9.09 % for the DOI. The error occurred in the sections where the DOI position changed, such as 5 mm and 15 mm.

4. Conclusion

We designed a cost-effective and MRI compatible detector using cross point and dual-ended readout methods with WLS fibers and MPPCs as semiconductor photosensors for high resolution. The three-dimensional positions for four DOI layers using two crystal layers were directly acquired through a convergence of cross point readout and dual-ended readout methods. Since the depth information can be measured in two layers with a single layer of scintillation crystal, when the crystal is composed of several layers, the depth information can be measured at twice the scintillation layer. Therefore, spatial resolution can be further improved when designing the detector using multiple layers of scintillation crystal. This method reduces the number of MPPCs required compared to the cross point readout method alone. The accuracy of pixel identification was high, over 90 % for thresholds between 10 % and 80 % in all crystal pixels. The DOI positioning accuracy also was high (about 90 %). Thus, our approach is promising for use in preclinical PET-MRI systems because of the low cost and high performance of digital three-dimensional positioning in all crystal pixels without being affected by the magnetic field.

Acknowledgements

This research was supported by the National Foundation of korea (NRF) funded by the Ministry of Education, Science and Technolgoy (2017R1C1B5018415).

References

[1] G. Stortz, J. D. Thiessen, D. Bishop, M. S. Khan, P. Kozlowski, F. Retiere, G. Schellenberg, E. Shams, X. Zhang, C. J. Thompson, A. L. Goertzen, and V. Sossi, J. Nucl. Med. **59**, 3 (2018).
[2] C. Catana, Y. Wu, M. S. Judenhofer, J. Qi, B. J. Pichler, and S. R. Cherry, J. Nucl. Med. **47**, 12 (2006).
[3] D. P. McElroy, V. Saveliev, A. Reznik, AND J. A. Rowlands, Nucl. Inst. Meth. A **571** (2007).
[4] J. Wehner, B. Weissler, P. Dueppenbecker, P. Gebhardt, D. Schug, W. Ruetten, F. Kiessling, and V. Schulz, Nucl. Inst. Meth. A **734** (2014).
[5] B. H. Peng and C. S. Levin, Curr. Pharm. Biotechnol. **11**, 6 (2010).
[6] R. S. Miyaoka, T. K. Lewellen, H. Yu, and D. L. McDaniel, IEEE Trans. Nucl. Sci. **45**, 3 (1998).
[7] W. W. Moses, Nucl. Inst. Meth. A **648**, Supplement 1 (2011).
[8] M. Ito, S. J. Hong, and J. S. Lee, Biomed. Eng. Lett. **1** (2011).
[9] L. R. MacDonald and M. Dahlbom, IEEE Trans. Nucl. Sci. **45**, 4 (1998).
[10] J. H. Jung, Y. Choi, Y. H. Chung, O. Devroede, M. Krieguer, P. Bruyndonckx, and S. Tavernier, Nucl. Inst. Meth. A **571** (2007).
[11] A. Vandenbroucke, A. M. K. Foudray, P. D. Olcott, and C. S. Levin, Phys. Med. Biol. **55**, 19 (2010).
[12] Y. Shao, R. W. Silverman, R. Farrell, L. Cirignano, R. Grazioso, K. S. Shah, G. Visser, M. Clajus, T. O. Tumer, and S. R. Cherry, IEEE Trans. Nucl. Sci. **47**, 3 (2000).
[13] S.-J. Lee and C-H. Baek, Nucl. Inst. Meth. A **887** (2018).
[14] F. Cayouette, D. Laurendeau, and C. Moisan, Proceeding SPIE **4833** (2003).
[15] https://www.crystals.saint-gobain.com/products/scintillating-fiber
[16] http://www.hamamatsu.com.cn/UserFiles/DownFile/Product/s12572-025_etc_kapd1043e03.pdf
[17] J. H. Lee, S.-J. Lee, S. J. An, H.-I. K, and Y. H. Chung, J. Kor. Phys. Soc. **68**, 9 (2016).